# Journal of Materials Chemistry A

Accepted Manuscript


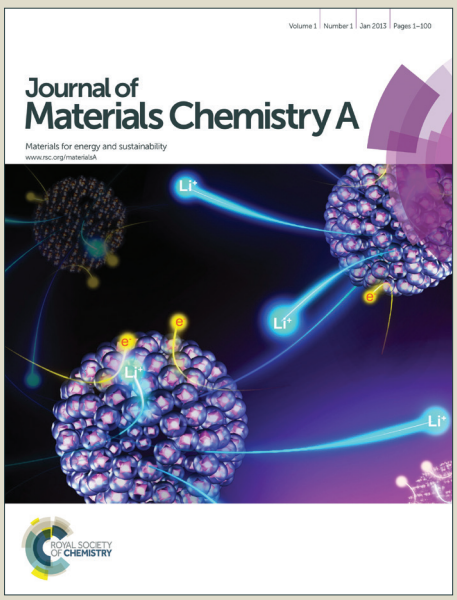





ROYAL SOCIETY OF CHEMISTRY

www.rsc.org/materialsA

**Sandwich nanoarchitecture of $LiV_3O_8$/graphene multilayer nanomembranes via layer-by-layer self-assembly for long-cycle-life lithium-ion battery cathodes**

By *Runwei Mo*[1,2]*, *Ying Du*[1], *Zhengyu Lei*[1], *David Rooney*[3] and *Kening Sun*[1]*

[1] Academy of Fundamental and Interdisciplinary Sciences, Harbin Institute of Technology, Harbin 150001, (China)
E-mail: keningsunhit@126.com
[2] State Key Laboratory of Functional Materials for Informatics, Shanghai Institute of Microsystem and Information Technology, Shanghai, 20050, (China)
E-mail: rwmo@mail.sim.ac.cn
[3] School of Chemistry and Chemical Engineering, Queen's University Belfast, Belfast, BT9 5AG, (Northern Ireland)

## Introduction

Rechargeable lithium ion batteries (LIBs) with high energy density and long cycling lifespan are needed to power future advanced communications equipment and electric vehicles.[1-5] However a lack of high performance cathode materials has become a technological bottleneck for the commercial development of such devices.[6] Lithium trivanadate materials,[7-14] $LiV_3O_8$, have attracted much attention due to their encouraging features such as high specific capacity (ca. 380 mA h $g^{-1}$) and low cost. Despite these advantages, one major weakness of $LiV_3O_8$ is their intrinsically poor rate capability, which has been recently verified to be associated with its low electronic conductivity and Li ion diffusion rate.[9-11] In addition, these materials suffer from fragile surface properties at high potential, erosion from the electrolytes, and dissolution of vanadium.[12-14] Therefore, implementation of layered lithium trivanadate materials which could achieve high and stable capacity at high rates has not really been feasible.

Numerous electrodes designs have been developed to improve the overall electrochemical performance of $LiV_3O_8$ cathodes. One strategy is to use $LiV_3O_8$ nanostructures of various morphologies, such as $LiV_3O_8$ nanocrystals,[15,16] $LiV_3O_8$ nanorods[17,18] and $LiV_3O_8$ nanosheets.[19] These nanostructures facilitate the electron transport along the long dimension and $Li^+$ insertion/extraction along the lateral direction. A recent design of LIB cathodes, consisting of nanosheet-structured $LiV_3O_8$ electrodes prepared by adding an appropriate polymer, was capable of charging/discharging for 166 mAh $g^{-1}$ at current densities of 1 A $g^{-1}$.[19] Another effective strategy is to use surface modification to reinforce the rate performance and cycling stability of layered lithium trivanadate materials. It has been shown that coating lithium trivanadate materials with various oxides and phosphates could stabilize the surface structure of the materials.[20-23] For example, lithium trivanadate materials coated with $Al_2O_3$ showed a reversible capacity of 139 mAh $g^{-1}$ at current densities of 1.5 A $g^{-1}$.[23] Recently, graphene has shown great potential in Li ion battery cathodes because of its high conductivity, light weight nature, high mechanical strength, and structural flexibility.[24-26] Such characteristics may also play an important role in enhancing the electrochemical performance of cathode materials.[27-30] Our previous report noted that $LiV_3O_8$ nanorod/graphene nanocomposites fabricated by in-situ synthesis showed a high reversible capacity in LIBs cathode applications.[31] However, there is still a need for well-designed $LiV_3O_8$-based nanomaterials and their facile synthetic methods towards high-performance cathode materials.

Here we report on a novel sandwich nanoarchitecture of $LiV_3O_8$/Graphene

multilayer nanomembranes, namely, layer-by-layer self-assembly of alternating sandwich nanoarchitecture of multilayered nanosized $LiV_3O_8$/ Graphene nanosheets (M-nLVO/GNs) on a porous Ni foam (Figure 1). This was made using layer-by-layer self-assembly which has been proven to generate multilayer nanomembranes with desirable functionality including highly controlled nano- and micron-scale organization.[32,33] Importantly, one can combine mechanical properties, electrical conductivity and ionic transport in LBL-made materials better than in other composites.[34-36] In this contribution, the sandwich nanoarchitecture of LVO/GNs multilayer nanomembranes is designed by combining the merits of nanomembranes and GNs protecting layer, which demonstrates good capacity retention and long cycling life as cathode materials for LIBs. In addition, Layer-by-layer assembly enables the preparation of conformal thin films onto virtually any substrate, irrespective of its size or shape, further expanding its potential by creating 3D objects beyond traditional thin films on flat 2D surfaces.

## Experimental Section

### Synthesis of graphene oxide (GO)

The graphite oxide was synthesized from natural graphite flake (Alfa Aesar, 325 mesh) by a modified Hummers method.[37,38] As-prepared graphite oxide was dispersed in water by ultrasonication for 30 min, followed by a low-speed centrifugation to remove any aggregated GO. This provided a homogeneous GO aqueous dispersion (1 mg $mL^{-1}$) suitable for further use.

### Synthesis of nanosized $LiV_3O_8$ powders (nLVO)

In a typical experimental procedure, 6.2 g of Cetyltrimethyl Ammonium Bromide (CTAB) was dissolved in a mixture of 10 ml of n-pentanol and 60 ml of n-hexane. Then, 10 ml of water solution was slowly added and the mixture intensely stirred for 20 min at room temperature resulting in the formation of a transparent water-in-oil emulsion. Then 1.8 mmol of $NH_4VO_3$ and 2 mmol of $H_2C_2O_4$ or 1 mmol of $LiOH{\cdot}H_2O$ was added to this transparent water-in-oil emulsion while stirring. After 10 min of vigorous agitation, equivalent volumes of two separate microemulsion solutions containing $NH_4VO_3$ and $H_2C_2O_4$ or $LiOH{\cdot}H_2O$ were mixed rapidly. The suspension of the microemulsion was transferred into stainless steel autoclaves and heated at 200 °C for 16 h, followed by cooling to room temperature naturally. After cooling to ambient temperature, the black precipate was obtained by centrifugation, and washed several times with distilled water. After drying in a vacuum oven at 70 °C overnight the as-synthesized $LiV_3O_8$ was annealed at 400 °C for 2 h in a nitrogen flow in order to remove residual water molecules and improve the crystallinity of $LiV_3O_8$ in the obtained composites, which would further improve its electrochemical performance.

**Modification of nanosized $LiV_3O_8$ and Ni foam**

In a typical experimental procedure, as-synthesized nanosized $LiV_3O_8$ (500 mg) and 20 wt% poly(diallydimethylammonium chloride) (PDDA) (2.0 g, Aldrich, Mw<500 000 Da) aqueous solution were dispersed in water (150 mL) by sonication in a water bath for 5 min, respectively. The excess PDDA was removed by four repeated centrifugation (12,000 rpm)/wash/redispersion cycles. Then, the obtained

PDDA-modified nLVO aqueous solution was diluted to 500 mL with double-distilled water. The PDDA-modified nLVO were positively charged.

A porous Ni foam (Diameter: 12.6 mm, Thickness: 0.28mm) was immersed into 20 wt% PDDA aqueous solution dispersed in water (150 mL) for 5 min. Then the Ni foam was taken out from the PDDA aqueous solution and dried. The PDDA-modified Ni foam was also positively charged.

**Layer-by-layer self-assembly of alternating sandwich nanoarchitecture of LVO/GNs multilayer nanomembranes on porous Ni foams (M-nLVO/GNs)**

For fabrication of a M-nLVO/GNs, the as-prepared PDDA-modified Ni foam was soaked into the as-obtained graphene oxide (GO) aqueous dispersion (500 mL) for 10 min. Then the PDDA/GO-modified Ni foam was soaked in the as-obtained obtained PDDA-modified nLVO aqueous solution (500 mL) for 10 min. During each adsorption step, the foil was rinsed with DI water and dried. A multilayered electrode was obtained by this Layer-by-layer assembly process. Finally, the products were annealed at 600 $^{o}$C in air for 5 h to ultimately achieve the M-nLVO/GNs hybrid electrode. For fabrication of a pure M-nLVO electrode, the Ni foam was dipped into an nLVO dispersion and then taken out. The nLVO covered the entire Ni foam after drying. We repeated this multiple times in order to obtain the M-nLVO electrodes. To obtain the weight of active materials, the Ni foam was weighed before and after the annealing process. The prepared M-nLVO/GNs hybrid electrode consisted of 8-layer nLVO films and 8-layer GO films, and the total active material (nLVO and GNs) weight of the cathode material was 2.2 mg.

**Material Characterizations**

XRD measurements were conducted on a Rigaku D/max-B diffractometer using Cu Kα radiation at a scanning rate of 2° $min^{-1}$ in the range of 5-60°. Zeta-potential measurements were measured by an electrophoretic light scattering and dynamic light scattering spectrophotometer (DelsaNano C). Morphology of products was characterized by scanning electron microscopy (SEM, Hitachi S4800) and TEM and HRTEMhigh (JEM-2100) with an accelerating voltage of 200 KV. Additionally, Raman were recorded on an inVia Raman microprobe with 633 nm laser with 10% intensity to determine the extent of graphitic disorder.

**Electrochemical measurements**

Coin cells (2032-tpye) were assembled in an argon-filled glove box with the quantity of oxygen and moisture below 1 ppm. The M-nLVO/GNs hybrid electrode were integrated into two-electrode CR2025-type coin cells for electrochemical measurements, metallic lithium foil was used as the counter electrode and porous polypropylene films as the separator. The electrolyte was 1 M $LiPF_6$ dissolved in ethylene carbonate (EC) and dimethyl carbonate (DMC) and diethyl carbonate (DEC) at a volumetric ratio of 1:1:1. The discharge-charge tests were conducted at various rates within a voltage window from 1.5 V to 4.0 V (vs. $Li^+/Li$) on the BTS battery testing system (Neware, Shenzhen, China). Electrical impedance spectroscopy (EIS) experiments were carried out on a Parstat 2273 advanced electrochemical system in the frequency range mainly from 100 kHz to 10 mHz with the a.c. signal amplitude of 5 mV.

**Results and discussion**

As shown in figure 1, the fabrication procedure is primarily based on an layer-by-layer self-assembly method for alternating sandwich nanoarchitecture of M-nLVO/GNs hybrid electrodes. Firstly, poly(diallyldimethylammonium chloride (PDDA) (see Figure S1, in the Supporting Information) was used to induce a positive surface charge of the Ni foam as well as the nanosized $LiV_3O_8$ (nLVO) as shown in Figure 1b,d (PDDA-modified Ni foam and PDDA-modified nLVO). The second step combined the positively charged Ni foam assemble with a negatively charged well-dispersed GO suspension (Figure S2) resulting in an electrostatic attraction between the GO and the modified foam (PDDA/GO-modified Ni foam). Hence the GO nanosheets were coated on the porous surface of the Ni foam as shown in Figure 1e. Thirdly, the now negatively charged PDDA/GO-modified Ni foam assemble was modified using the positively charged PDDA-modified nLVO (Figure 1f). Therefore, multilayered electrodes could be obtained by alternating deposition of GO and nLVO layers (Figure 1g). To survey the assembly process, we carried out zeta potential measurements. The results show the zeta potentials of PDDA-modified Ni foam, GO and PDDA-modified nLVO are +42 mV, -56 mV, and +45 mV, respectively. The surface potential of PDDA-modified Ni foam was found to periodically vary from -39.2 ± 7.8 (from the first GO layer) to +49.3 ± 13.6 mV (for the last nLVO-PDDA layer) (Figure S3). After drying and thermal reduction under nitrogen flow, the PDDA had decomposed almost completely.[39] Simultaneously, GO was reduced to GNs under these thermal conditions. Finally, the M-nLVO/GNs hybrid electrode was obtained

(Figure 1h).

The sandwich nanoarchitecture of M-nLVO/GNs hybrid electrodes were characterized by scanning electron microscopy (SEM) and Transmission electron microscopy (TEM). Figure 2a shows an SEM image of the resulting cathode with an average Ni foam pore size of 400 μm, demonstrating an interconnected network of Ni structures, which facilitates fast transfer of electrons during lithiation and delithiation. The EDS spectrum from the SEM, shown in Figure S4, certifies the presence and proportion of C, V, O and Ni, arising from the Ni substrate. Here we used nLVO with a diameter of around 20 nm in the electrodes. The GNs layers covered on the surface of nLVO are shown in Figure 2b. Two layers of nLVO are observed with two layers of GNs between them (Figure 2c), where the GNs layer can be easily observed from its wrinkles between the nLVO layers (marked by arrows). Figure 2d,e shows an TEM image of the M-nLVO NPs/GNs hybrid electrode. At least three layers of nLVO could be identified with GNs layers in between. The selected area electronic diffraction pattern (inset in Figure 2e) corresponding to M-nLVO/GNs gives a set of diffraction rings, which can be clearly assigned to the diffractions of the {100}, {002}, {-111}, and {103} planes, respectively, of the layered-type structure of $LiV_3O_8$. This result is consistent with the XRD characterization where the refractions of these planes are intensified (Figure S5). This electrostatic self-assembly of the multilayered structures not only improves the electronic conductivity of nLVO, but also appeared to exhibit strong interactions, maintaining excellent cycling performance in LIBs applications. Raman spectroscopy is a widely used tool for the characterization of carbon materials,

especially considering the fact that double carbon-carbon bonds lead to high Raman intensities.[40] The Raman spectrum from 400 to 2000 $cm^{-1}$ is displayed in Figure 2f. Clearly, four distinct peaks are observed at 768, 992, 1329, and 1592 $cm^{-1}$, which are associated with LVO and GNs. The GNs exhibit a disordered band (D-band) at 1329 $cm^{-1}$ and a strong tangential mode band (G-band) at 1592 $cm^{-1}$.[41] We found that intensities of D and G peaks are similar, indicating that the GNs contain a large amount of disordered $sp^2$ carbons (a large number of defects). The defects on GNs generated during the fabrication process (e.g., oxidation and reduction) could provide Li diffusion channels,[42] and allow electrolytes to penetrate easily into the GNs and react electrochemically with nLVO during the charge/discharge process. The Raman shift of $LiV_3O_8$ sample at 992 $cm^{-1}$ is attributed to the V=O stretching vibrations of $VO_5$ pyramids, and the band at 768 $cm^{-1}$ is assigned to the atomic motions of corner-sharing oxygen atoms among the $VO_6$, $VO_5$, and $LiO_6$ polyhedrons as identified in previous literature.[43]

To explore the advantages of the M-nLVO/GNs hybrid electrode as a cathode for LIBs, we firstly investigated its initial charge/discharge performance between 1.5 and 4.0 V at current densities of 0.3 A $g^{-1}$ (1 C) as shown in Figure 3a. It is apparent that the curves of all the electrodes share a resemblance, the apparent three discharge plateaus located at 2.8, 2.6 and 2.3V, as previously reported,[44] can be well identified. The 2.8V discharge plateau represents an electrochemical signature of single-phase insertion process, and the 2.6V plateau is a signature of the two-phase transformation between $Li_{1+x}V_3O_8$ ($1 \leq x \leq 2$) and $Li_4V_3O_8$, while the last 2.3V process concerns a

slower kinetic insertion process.[45-47] For comparison, we also carried out similar tests on M-nLVO electrode synthesized without GNs (Figure S6). The nLVO are spherical, and there are aggregates in the large visual fields. As shown in Figure 3a a first specific discharge capacity as high as 235 mA h $g^{-1}$ is observed on M-nLVO/GNs hybrid electrodes at current densities of 0.3 A $g^{-1}$ based on the mass of the active material nLVO and GNs, which is much higher than that of M-nLVO electrodes (160 mA h $g^{-1}$). Figure S7 shows the discharge/charge curves at the first, fifth, fiftieth, one-hundredth and three-hundredth cycles for the M-nLVO electrode. Surprisingly, under a current density of 0.3 A $g^{-1}$, the M-nLVO electrodes electrode delivered ca. 211 mAh $g^{-1}$ with 90 % capacity retention at the 300$^{th}$ cycle (Figure 3b). It should be noted that the coulombic efficiencies are about 98% during cycling at current densities of 0.3 A $g^{-1}$ as shown in Figure 3b. The M-nLVO electrode shows much faster capacity fading, up to 32% during 150 cycles. Therefore, the M-nLVO/GNs hybrid electrode displays remarkably superior capacity retention, which can be attributed to the unique architecture of the M-nLVO/GNs hybrid electrode where the GNs layer can effectively prevent aggregation of nLVO and offers a more stable and robust structure at high potential, lower erosion, and decreased vanadium dissolution in the electrolyte.

The poor rate performance of the layered lithium trivanadate materials is one of the major barriers to their applications in future advanced communications equipment and electric vehicles. Our work has provided evidence that high-rate discharge capacities could be achieved by the M-nLVO/GNs hybrid electrodes as shown in

Figure 3c. The reversible capacity of M-nLVO/GNs hybrid electrode stabilizes at 266 mA h $g^{-1}$ after 20 cycles at current densities of 0.1 A $g^{-1}$. Upon higher discharge-charge current densities at 0.3, 1, 3, 5 and 10 A $g^{-1}$, its reversible capacities are maintained at 221, 180, 122, 90 and 57 mA h $g^{-1}$, respectively. Importantly, after the high rate measurements, the specific capacity of M-nLVO/GNs hybrid electrode at current densities of 0.1 A $g^{-1}$ can recover to their initial value, indicating its high reversibility. Compared with the excellent rate performance of the M-nLVO/GNs hybrid electrode, the rate performance of the M-nLVO electrode is very poor. To further investigate the capacity stability, the M-nLVO/GNs hybrid electrode cathode was also tested at current densities of 4 and 8 A $g^{-1}$ for 300 cycles. The initial charge/discharge performance between 1.5 and 4.0 V at current densities of 0.4 and 8 A $g^{-1}$ as shown in FigureS8. It is worth noting that the capacity can also remain at 105 and 70 mAh $g^{-1}$ without significant fading, as shown in Figure 4a. The coulombic efficiency reaches 98% after the first several cycles, indicating a good reversibility of the M-nLVO/GNs hybrid electrode. More importantly, the robust structure and morphology of M-nLVO/GNs hybrid electrodes at current densities of 8 A $g^{-1}$ after 300 cycles is still well retained (Figure 4b). The excellent high-rate performance is attributed to the substantial decrease in charge-transfer resistance due to the unique structure of the M-nLVO/GNs hybrid electrode. Figure 3d compares the Nyquist plots of electrodes of M-nLVO/GNs and M-nLVO. In general, the semicircle is attributed to the summation of the contact, the solid-electrolyte interphase resistance, and the charge-transfer resistance, while the inclined line at ca. 45$^{o}$ angle to the real axis

corresponds to the lithium-diffusion process within the electrodes. The impedance spectra are fitted with an equivalent circuit, where the symbols, $R_s$, $R_f$, $R_{ct}$,and $Z_w$, denote the solution resistance, contact resistance, charge-transfer resistance and Warburg impedance, respectively. Apparently, the fitting results of $R_s$, $R_f$, and $R_{ct}$ of Sample M-nLVO/GNs and M-nLVO (shown in Figure S9 and Table S1, ESI†) indicate that the $R_f$ and $R_{ct}$ values of M-nLVO/GNs hybrid electrode are smaller than the M-nLVO electrode, indicating that the interconnected, porous GNs layers provide a conductive network for electronic transport from nLVO within the whole electrode and thus decreases resistance.

Consequently, the excellent cycling performance and rate performance of M-nLVO/GNs hybrid electrodes may be caused by the synergistic coupling effects in the multilayered LVO/GNs sandwich nanostructures (Figure 4c). The newly-designed sandwich nanostructures offer several advantages as LIBs cathodes. i) Compared with the conventional Al current collector, the 3D porous Ni foam can improve electron transport from the active materials to the current collector via the networks and extensive contacts with the electrolyte. This results in a fast and easy access of electrolyte ions to the surface of the active materials, reducing the diffusion resistance of the electrolyte; ii) Reduction of the active materials particle size to nanoscale levels can improve the rate performance of electrode material by shortening the lithium-diffusion pathways; iii) The interconnected, porous GNs layers provide a conductive network for electronic transport, which improves the electrical conductivity, rate capability, and usage of nLVO; iv) Electrostatic self-assembly of

alternating multilayered structures appeared to effectively prevent aggregation of nLVO and offers a more stable structure with robust surface properties at high potential, lowering erosion from the electrolytes, and decreasing the amount of vanadium dissolved in the electrolyte. Both of these are beneficial for maintaining the stability of the LVO cathode and improving its cyclability. It is anticipated that the M-nLVO/GNs hybrid electrodes could not only effectively overcome existing challenges of LVO-based cathodes and allow for the fabrication of high-capacity stable cathodes with rapid charging capability, but also as cathode materials by electrostatic self-assembly without the need for conductive additives and binder, which enhances the energy density. Therefore, the results of preliminary experiments on the layer-by-layer self-assembly of alternating the sandwich nanoarchitecture of M-nLVO/GNs hybrid electrode can provide a new possibility of preparation of other graphene-based composites.

**Conclusions**

In conclusion, the sandwich nanoarchitecture of LVO/GNs multilayer nanomembranes are designed via layer-by-layer self-assembly strategy, and exhibit long cycling lifetime of 300 cycles at 0.3 A $g^{-1}$ with a capacity degradation of only 3.3% per 100 cycles as cathde for LIBs. The sandwich nanoarchitecture hybrid electrode with outmost graphene clothing provides a strong structural buffer, high electrical conductivity, which reveals a new approach to solving an old problem of cycling stability, providing a scalable methodology for treating commercial cathode. The layer-by-layer self-assembly fabrication of layered alternating multilayered

sandwich nanostructures is easy to scale up, and holds great potential for application of the next-generation Li-ion batteries. Very significantly, this novel insight into the design and synthesis of multilayered sandwich nanoarchitecture would extend their application to various electrochemical energy storage devices, such as fuel cells and supercapacitors.

## Acknowledgments

This work was financially supported by National Natural Science Foundation of China (NSFC 21076023), Jiangsu Province Cultivation base for State Key Laboratory of Photovoltaic Science and Technology (201508), China Post-doctoral Science Foundation(2011M500650).

## References

1 M. Armand and J. M. Tarascon, *Nature.*, 2008, **451**, 652.

2 B. Dunn, H. Kamath and J. M. Tarascon, *Science.*, 2011, **334**, 928.

3 J. B. Goodenough and K. S. Park, *J. Am. Chem. Soc.*, 2013, **135**, 1167.

4 M. S. Whittingham, *Chem. Rev.*, 2004, **104**, 4271.

5 W. C. Duan, Z. Hu, K. Zhang, F. Y. Cheng, Z. L. Tao and J. Chen, *Nanoscale*., 2013, **5**, 6485.

6 N. S. Choi, Z. Chen, S. A. Freunberger, X. Ji, Y. K. Sun, K. Amine, G. Yushin, L. F. Nazar, J. Cho and P. G. Bruce, *Angew. Chem. Int. Ed.*, 2012, **51**, 9994.

7 K. Westa, B. Zachau-Christiansena, S. Skaarupb, Y. Saidic, J. Barkerc, I. I. Olsenc, R. Pynenburgc and R. Koksbang, *J. Electrochem. Soc.*, 1996, **143**, 820.

8 G. Q. Liu, C. L. Zeng and K. Yang, *Electrochim. Acta.*, 2002, **47**, 3239.

9 M. Dubarry, J. Gaubicher, D. Guyomard, N. Steunou and J. Livage, *Chem. Mater.*, 2004, **16**,

4867-4869.

10 Q. Shi, R. Z. Hu, M. Q. Zeng and M. Zhu, *Electrochim. Acta*., 2010, **55**, 6645.

11 G. Yang, G. Wang and W. H. Hou, *J. Phys. Chem. B.*, 2005, **109**, 11186.

12 H. L. Zhang, J. R. Neilson and D. E. Morse, *J. Phys. Chem. C.*, 2010, **114**, 19550.

13 L. Liang, M. Zhou and Y. Xie, *Chem. Asi. J.*, 2012, **7**, 565.

14 S. H. Choi and Y. C. Kang, *Chem. Eur. J.*, 2013, **19**, 17305.

15 Q. Shi, R. Z. Hu, L. Z. Ouyang, M. Q. Zeng and M. Zhu, *Electrochem. Commun*., 2009, **11**, 2169.

16 X. H. Xiong, Z. X. Wang, H. J. Guo, X. H. Li, F. X. Wu and P. Yue, *Electrochim. Acta.*, 2012, **71**, 206.

17 A. Q. Pan, J. Liu, J. G. Zhang, G. Z. Cao, W. Xu, Z. M. Nie, X. Jie, D. W. Choi, B. W. Arey, C. M. Wang and S. Q. Liang, *J. Mater. Chem.*, 2011, **21**, 1153.

18 Y. Q. Qiao, X. L. Wang, J. P. Zhou, J. Zhang, C. D. Gu and J. P. Tu, *J. Power Sources.*, 2012, **198**, 287.

19 A. Q. Pan, J. G. Zhang, G. Z. Cao, S. Q. Liang, C. M. Wang, Z. M. Nie, B. W. Arey, W. Xu, D. W. Liu, J. Xiao, G. S. Li and J. Liu, *J. Mater. Chem.*, 2011, **21**, 10077.

20 L. F. Jiao, L. Liu, J. L. Sun, L. Yang,Y. H. Zhang, H. T. Yuan, Y. M. Wang and X. D. Zhou, *J. Phys. Chem. C.*, 2008, **112**, 18249.

21 X. W. Gao, J. Z. Wang, S. L. Chou, H. K. Liu, *J. Power Sources.*, 2012, **220**, 47.

22 L. L. Liu, X. J. Wang, Y. S. Zhu, C. L. Hu, Y. P. Wu and R. Holze, *J. Power Sources.*, 2013, **224** , 290.

23 S. Huang, J. P. Tu, X. M. Jian, Y. Lu, S. J. Shi, X. Y. Zhao, T. Q. Wang, X. L. Wang and C. D. Gu, *J. Power Sources.*, 2014, **245**, 698.

24 S. Park and R. S. Ruoff, *Nat. Nanotechnol.*, 2009, **4**, 217.

25 H. Wang, J. T. Robinson, G. Diankov and H. Dai, *J. Am. Chem. Soc.*, 2010, **132**, 3270.

26 Y. Liang, H. Wang, H. S. Casalongue, Z. Chen, H. Dai, *Nano Res.*, 2010, **3**, 701.

27 H. D. Liu, P. Gao, J. H. Fang and G. Yang, *Chem. Commun*., 2011, **47**, 9110.

28 H. L. Wang, Y. Yang, Y. Y. Liang, L. F. Cui, H. S. Casalongue, Y. G. Li, G. S. Hong, Y. Cui and H. J. Dai, *Angew. Chem. Int. Ed*., 2011, **50**, 7364.

29 B. Wang, D. L. Wang, Q. M. Wang, T. F. Liu, C. F. Guo and X. S. Zhao, *J. Mater. Chem. A*.,

2013, **1**, 135.

30 L. H. Hu, F. Y. Wu, C. T. Lin, A. N. Khlobystov and L. J. Li, *Nat. Commun*., 2013, **4**, 1687.

31 R. W. Mo, Y. Du, N. Q. Zhang, D. Rooney and K. N. Sun, *Chem. Commun*., 2013, **49**, 9143.

32 S. W. Lee, B. M. Gallant, H. R. Byon, P. T. Hammond and Y. S. Horn, *Energy Environ. Sci*., 2011, **4**, 1972.

33 B. S. Shim, J. Zhu, E. Jan, K. Critchley and N. A. Kotov, *ACS Nano*., 2010, **4**, 3725.

34 M. N. Hyder, B. M. Gallant, N. J. Shah, Y. S. Horn and P. T. Hammond, *Nano Lett*., 2013, **13**, 4610.

35 M. N. Hyder, S. W. Lee, F. C. Cebeci, D. J. Schmidt, Y. S. Horn and P. T. Hammond, *ACS Nano*., 2011, **5**, 8552.

36 J. Zhu, H. N. Zhang and N. A. Kotov, *ACS Nano*., 2013, **7**, 4818.

37 Y. Chen, X. Zhang, P. Yu and Y. W. Ma, *Chem. Commun*., 2009, 4527.

38 C. H. Xu, J. Sun and L. Gao, *J. Mater. Chem*., 2011, **21**, 11253.

39 F. F. Xia, X. L. Hu, Y. M. Sun, W. Luo and Y. H. Huang, *Nanoscale*., 2012, **4**, 4707.

40 G. X. Wang, X. P. Shen, J. Yao and J. Park, *Carbon*., 2009, **47**, 2049.

41 S. Stankovich, D. A. Dikin, R. D. Piner, K. A. Kohlhaas, A. Kleinhammes, Y. Jia, Y. Wu, S. B. T. Nguyen and R. S. Ruoff, *Carbon*., 2007, **45**, 1558.

42 K. Erickson, R. Erni, Z. Lee, N. Alem and W. Gannett, *Adv. Mater*., 2010, **22**, 4467.

43 X. Zhang and R. Frech, *Electrochim. Acta*., 1998, **43**, 861.

44 H. M. Liu, Y. G. Wang, K. X. Wang, Y. R. Wang and H. S. Zhou, *J. Power Sources*., 2009, **192**, 668.

45 J. Kawakita, T. Miura and T. Kishi, *J. Power Sources*., 1999, **83**, 79.

46 J. Kawakita, T. Miura and T. Kishi, *Solid State Ionics*., 1999, **120**, 109.

47 J. Kawakita, Y. Katayama, T. Miura and T. Kishi, *Solid State Ionics*., 1998, **107**, 145.

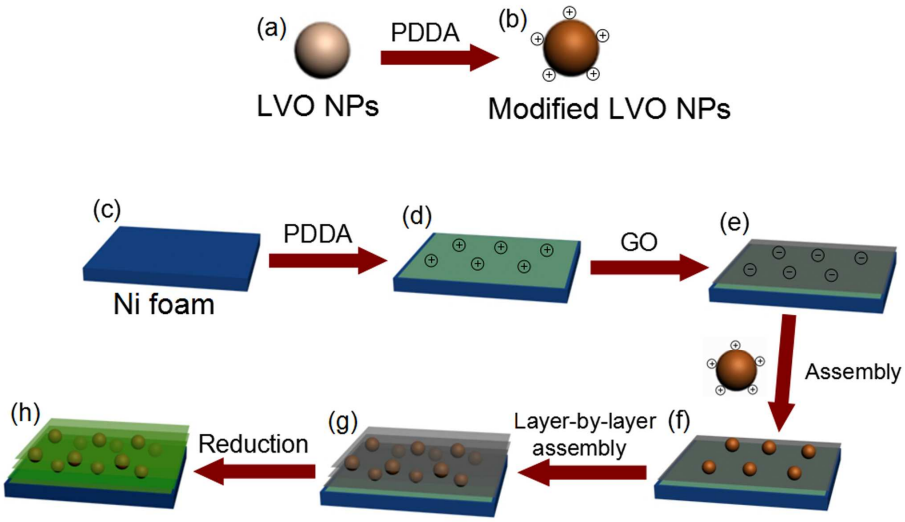


**Figure 1**. Schematic fabrication process for M-nLVO/GNs hybrid electrode. (a) Starting material LVO NPs. (b) Surface modification of PDDA on the LVO NPs. (c) Starting substrate material porous Ni foam. (d) Surface modification of PDDA on the porous Ni foam by immersing Ni foam in a PDDA aqueous suspension. (e) Deposition of GO sheets on the PDDA-modified Ni foam. (f) Deposition of PDDA-modified LVO NPs onto the GO-coated Ni foam using the self-assembly approach. (g) Multilayered structure with alternating LVO NP layers and GO layers obtained through layer-by-layer self-assembly. (h) Thermal reduction of GO at 600 °C for 5 h in a flow of Ar and $H_2$.

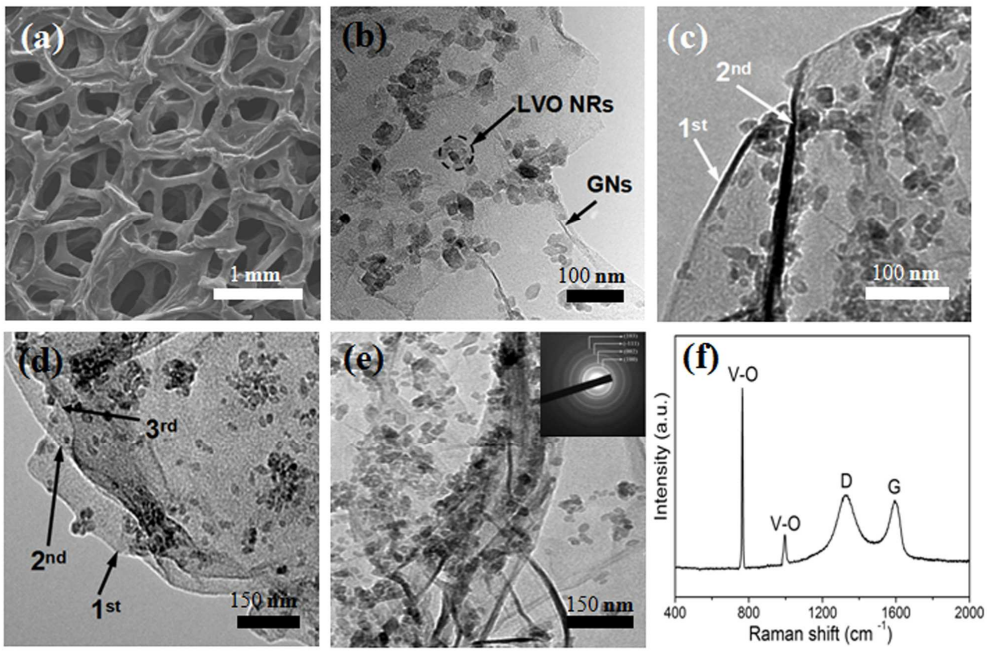


**Figure 2.** SEM and TEM images of the M-nLVO/GNs hybrid electrode fabricated by the electrostatic self-assembly method: (a) overview of the M-nLVO/GNs electrode; (b) a layer of GNs covering a layer of nLVO; (c) two layers of GNs covering two layers of nLVO; arrows indicate folds of GNs; (d) three layers of GNs covering three layers of nLVO (labelled as $1^{st}$, $2^{nd}$ , and $3^{rd}$ ); and (e) multilayer nLVO separated by GNs layers. (f) Raman spectrum of the M-nLVO/GNs hybrid electrode.

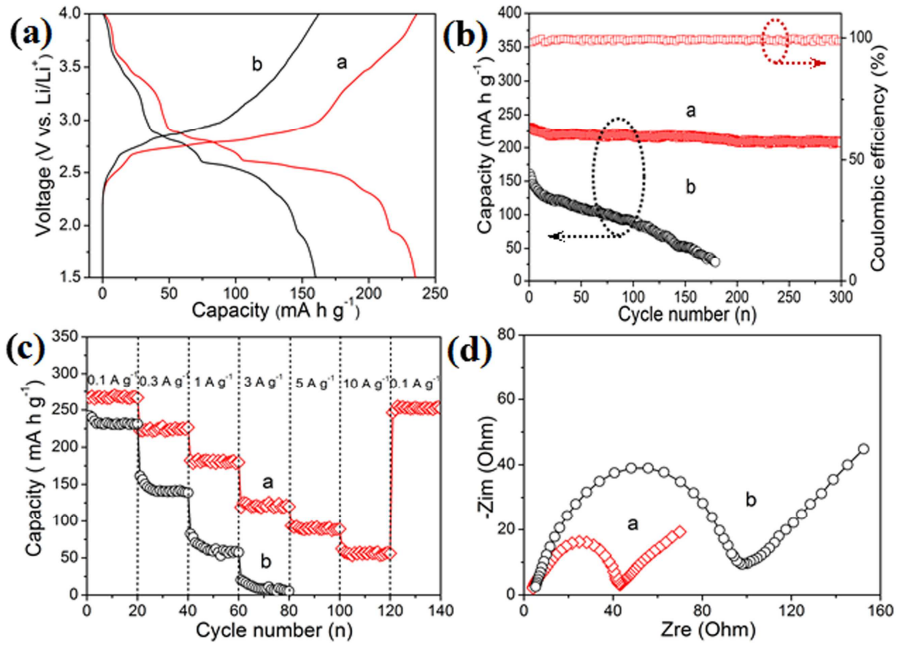


**Figure 3.** Electrochemical characteristics of the M-nLVO/GNs hybrid electrode. (a) First-cycle discharge curves of the M-nLVO/GNs and M-nLVO electrodes. (b) Left axis: cycling performance of the electrodes: M-nLVO/GNs and M-nLVO electrodes. The electrodes were charged-discharged between 1.5 and 4 V (vs. $Li/Li^+$) at current densities of 0.3 A $g^{-1}$ (1 C); Right axis: Coulombic efficiency of the M-nLVO/GNs hybrid electrode. (c) Rate-performance of the electrodes: M-nLVO/GNs and M-nLVO electrodes. (d) Nyquist plots of the M-nLVO/GNs and M-nLVO electrodes.

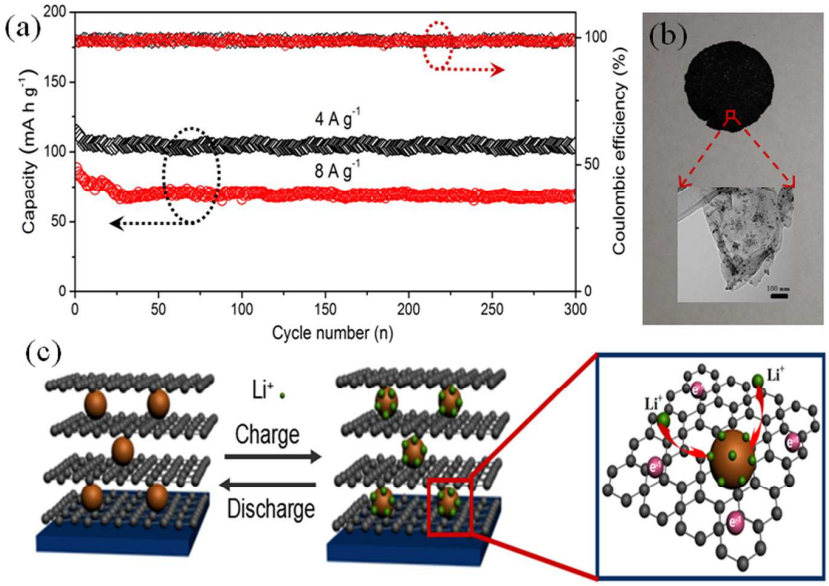


**Figure 4.** (a) Left axis: cycling performance of the M-nLVO/GNs hybrid electrode at current densities of 4 A $g^{-1}$ and 8 A $g^{-1}$, respectively. Right axis: coulombic efficiency of the M-nLVO/GNs hybrid electrode at current densities of 4 A $g^{-1}$ and 8 A $g^{-1}$, respectively. (b) Photograph of M-nLVO/GNs hybrid electrode (top), and TEM image of M-nLVO/GNs (bottom) after 300 discharge/charge cycles at current densities of 8 A $g^{-1}$. (c) Schematic drawing of the charge/discharge processes of the M-nLVO/GNs hybrid electrode cathode.